ARTICLES
https://doi.org/10.1038/s41588-018-0254-1
nature genetics

Identification of phagocytosis regulators using magnetic genome-wide CRISPR screens

Michael S. Haney[1,8], Christopher J. Bohlen[2,7,8*], David W. Morgens[1], James A. Ousey[1], Amira A. Barkal[3], C. Kimberly Tsui[1], Braeden K. Ego[1], Roni Levin[4], Roarke A. Kamber[1], Hannah Collins[2], Andrew Tucker[2], Amy Li[1], Daan Vorselen[5], Lorenzo Labitigan[5], Emily Crane[1], Evan Boyle[1], Lihua Jiang[1], Joanne Chan[1], Esther Rincón[6], William J. Greenleaf[1], Billy Li[1], Michael P. Snyder[1], Irving L. Weissman[3], Julie A. Theriot[5], Sean R. Collins[6], Ben A. Barres[2] and Michael C. Bassik[1*]

Phagocytosis is required for a broad range of physiological functions, from pathogen defense to tissue homeostasis, but the mechanisms required for phagocytosis of diverse substrates remain incompletely understood. Here, we developed a rapid magnet-based phenotypic screening strategy, and performed eight genome-wide CRISPR screens in human cells to identify genes regulating phagocytosis of distinct substrates. After validating select hits in focused miniscreens, orthogonal assays and primary human macrophages, we show that (1) the previously uncharacterized gene *NHLRC2* is a central player in phagocytosis, regulating RhoA-Rac1 signaling cascades that control actin polymerization and filopodia formation, (2) very-long-chain fatty acids are essential for efficient phagocytosis of certain substrates and (3) the previously uncharacterized Alzheimer's disease–associated gene *TM2D3* can preferentially influence uptake of amyloid-β aggregates. These findings illuminate new regulators and core principles of phagocytosis, and more generally establish an efficient method for unbiased identification of cellular uptake mechanisms across diverse physiological and pathological contexts.

Phagocytosis has a critical role in neutralization and termination of pathogens[1], but it also contributes to a diverse range of developmental, homeostatic and noninfectious disease processes, including apoptotic cell clearance, senescent erythrocyte turnover, tumor surveillance, elimination of cellular debris after injury, and synaptic pruning[2–8]. Imbalances in phagocytosis by macrophages or other 'non-professional' phagocytes[9,10] can lead to autoimmunity, developmental deficits and buildup of toxic protein aggregates[2,4]. Phagocytes use distinct surface receptors and signaling cascades to engulf different types of particles[11], and elucidating additional molecules that make differential contributions across substrates will help enable narrowly targeted therapeutics for correcting phagocytosis defects in specific diseases.

Depending on the features of the substrate targeted for engulfment, phagocytes use a spectrum of signaling cascades to achieve rapid cytoskeletal reorganization and substrate ingestion[11–14]. Much of our understanding about the molecular basis of phagocytosis derives from forward genetic screens in model organisms. Classical apoptotic cell engulfment screens in *Caenorhabditis elegans* have identified (among other genes) phagocytic receptors *ced-1* and *ced-6* as well as key signaling intermediates, *ced-5* and *ced-10*, which activate the SCAR/WAVE complex during apoptotic cell clearance[15,16]. *Ced* gene human orthologs *DOCK1*, *CRK*, *ELMO1* and *RAC1* perform analogous signaling functions in mammalian SCAR/WAVE recruitment to activated phagocytic receptors[17,18]. Additional organismal forward-genetic screens conducted in fruit flies and zebrafish have both corroborated prior findings and provided new insights into regulation of phagocytosis[19–22]. RNA interference screens in cultured *Drosophila melanogaster* S2 cells have also identified numerous phagocytic regulators[23–26], although a systematic screen for regulators of phagocytosis in mammalian cells has not been reported.

The development of the CRISPR/Cas9 system[27–29] has enabled markedly improved genome-scale knockout screens with high precision in mammalian cells[30–37]. With an appropriate selection strategy, pooled CRISPR screens allow for effective and systematic interrogation of complex cellular processes. Although such screens have been used successfully in a number of cases, comparative analysis of genome-scale screens has been limited by the cost and effort required either to grow large panels of cells extensively or to perform FACS-based sorting, which can be expensive and time consuming.

Here, we describe a strategy for rapid selection of large-scale human cell populations using phagocytic ability as a direct readout. This strategy relies on magnetic separation of cells that have engulfed paramagnetic particles. We conducted eight distinct genome-wide CRISPR screens to investigate mechanisms of phagocytosis for distinct particle types in the macrophage-differentiated human myeloid cell line U937. Taken together, this work defines multiple pathways central to human cell phagocytosis, and demonstrates a generalizable strategy using magnetic separation to rapidly identify regulators of phagocytosis for diverse substrates.

[1]Department of Genetics and Stanford University Chemistry, Engineering and Medicine for Human Health (ChEM-H), Stanford University School of Medicine, Stanford, CA, USA. [2]Department of Neurobiology, Stanford University School of Medicine, Stanford, CA, USA. [3]Institute for Stem Cell Biology, Stanford University School of Medicine, Stanford, CA, USA. [4]Department of Biochemistry, University of Toronto, Toronto, Ontario, Canada. [5]Department of Biochemistry, Stanford University School of Medicine, Stanford, CA, USA. [6]Department of Microbiology and Molecular Genetics, University of California, Davis, Davis, CA, USA. [7]Present address: Department of Neuroscience, Genentech, South San Francisco, CA, USA. [8]These authors contributed equally: M. S. Haney, C. J. Bohlen. *e-mail: bohlenc@gene.com; bassik@stanford.edu

Results

A magnetic separation screen for phagocytosis regulators. To systematically investigate the requirements for phagocytosis of a wide range of substrates, we sought to leverage the power and efficiency of pooled CRISPR screening. We selected a human myeloid cell line with phagocytic activity, U937 cells[38], and optimized a differentiation protocol (Supplementary Fig. 1a–c) that allowed the cells to robustly phagocytose diverse types of particles in a manner that depended on actin dynamics and that could be inhibited by cytochalasin D (Supplementary Fig. 1d,e). We then generated a knockout pool of U937 cells by stably expressing Cas9 and introducing a ~200,000-element lentiviral library of single-guide RNAs (sgRNAs) targeting every protein-coding gene in the genome with ten distinct sgRNAs per gene and ~10,000 negative-control sgRNAs[32].

To directly probe the dynamic cellular process of phagocytosis, we developed a magnet-based selection strategy in which U937 cells were rapidly separated based on their capacity to phagocytose superparamagnetic substrates. After incubation with superparamagnetic particles, cells were passed through a uniform magnetic field that captured magnetized cells that ingested paramagnetic particles while nonmagnetized cells that did not phagocytose passed through (Fig. 1a). Magnet-bound cell fractions were highly enriched for phagocytosing cells, with a single superparamagnetic bead conferring sufficient magnetism to capture associated cells on the column (Fig. 1b). Pretreatment of cells with cytochalasin D prevented magnetic capture, suggesting that surface-associated but noningested particles were efficiently removed (Supplementary Fig. 1f).

Identification of known and novel phagocytosis regulators. Having established a phenotypic selection assay, we next performed a genome-wide screen for regulators of phagocytosis in duplicate. In our initial screen we exposed a pool (2.5×10^8 cells) of differentiated, Cas9-expressing U937 cells containing a genome-wide knockout library to 1.3 µm–diameter superparamagnetic beads for a duration (30 min) optimized to allow for subsequent capture of ~80% of the cells on the magnet. Each sorted fraction was preserved and processed separately, allowing direct comparison of sgRNA abundance in magnet-bound versus unbound cellular fractions within each replicate. Importantly, magnetic selection of the large number of cells required for screening was routinely completed in 1–2 h, at least an order of magnitude faster than fluorescence or survival-based selections at this scale.

After cell separation, sgRNA sequences were recovered from genomic DNA and sequenced to determine the relative enrichment of each sgRNA in bound versus unbound fractions. Gene-level effects were derived using casTLE[39], with top negative and positive regulators showing clear enrichment across multiple sgRNAs relative to the distribution of both nontargeting and safe-targeting negative-control sgRNAs (Fig. 1c). Analysis of replicate screen data for 1.3 µm–diameter carboxy-coated beads identified 85 genes at 10% false discovery rate (FDR), including genes that promote and inhibit particle uptake (Fig. 1d, Supplementary Fig. 1g and Supplementary Tables 1 and 2). Genes enriched in the unbound fraction (denoted by a negative effect score) lead to decreased particle uptake when disrupted, and therefore are normally necessary for efficient phagocytosis. Conversely, genes enriched in the bound fraction (denoted by a positive effect score) lead to increased particle uptake when disrupted, and therefore normally inhibit phagocytosis. Pathway analysis for the 85 genes discovered as hits in the 1.3 µm bead screen showed strong enrichment of Reactome pathway terms related to phagocytosis and actin polymerization (Fig. 1e and Supplementary Table 1). Indeed, identified genes encompassed a nearly complete actin polymerization cascade known to be essential for phagocytic cup formation, including *RAC1*, *DOCK2*, five members of the five-subunit SCAR/WAVE complex (*NCKAP1L*, *WASF2*, *ABI1*, *CYFIP1* and *BRK1*) and five members of the seven-subunit ARP2/3 complex (*ACTR2*, *ACTR3*, *ARPC2*, *ARPC3* and *ARPC4*; Supplementary Fig. 1g).

Beyond canonical phagocytosis machinery, the hits were enriched for biological pathway categories related to positive regulation of mTOR signaling (Fig. 1e, Supplementary Fig. 1g and Supplementary Table 1). The mTOR-associated Ragulator complex and its regulatory target, RagA, have recently been identified as strong modifiers of microglial phagocytic flux in a zebrafish screen[22], a finding supported by identification of RagA (*RRAGA*) and three of five members of the Ragulator complex (*LAMTOR2*, *LAMTOR3* and *LAMTOR4*) by our screen in human cells (Fig. 1e and Supplementary Fig. 1g). Additionally, our initial screen identified *NPRL2* of the RagA-inhibiting GATOR1 complex as a gene that promotes phagocytosis when disrupted (Supplementary Fig. 1g). In addition to known factors, unexpected hits involved in lipid metabolism and sialic acid biosynthesis and the poorly characterized genes *NHLRC2*, *TM2D1*, *TM2D2* and *TM2D3* represent some of the strongest genetic regulators of phagocytosis in this system, with either general or selective effects on particle uptake (Supplementary Fig. 1g).

Diverse screens find general and substrate-specific hits. To allow for magnetic selection of cells based on phagocytosis of additional substrates, we covalently conjugated 30 nm–diameter iron oxide nanoparticles (IONPs) to purified myelin, zymosan (yeast cell wall particles) and sheep red blood cells (RBCs) conjugated with either IgG (IgGRBC) or complement (CompRBC). We also sought to more directly address the function of particle size and charge in phagocytosis. To this end, we performed additional genome-wide screens using superparamagnetic beads of 0.43 µm diameter (SmallBeads), 4.3 µm diameter (BigBeads), as well as oppositely charged, cationic 1.3 µm–diameter beads (PosBeads) (Fig. 1a). Magnetic labeling and phagocytosis of each substrate were optimized for efficient separation of phagocytosing U937 cells (Fig. 1f, Supplementary Fig. 2a–j, Supplementary Table 3 and Supplementary Note). We conducted genome-wide phagocytosis screens for all eight substrates, each in duplicate. Screen hits were typically moderately to highly expressed by both differentiated U937 cells and primary human microglia (Supplementary Fig. 3a and Supplementary Table 4); this suggests that our approach identifies genes relevant for phagocytosis in U937 cells and primary macrophages.

To compare the highest-confidence phagocytosis regulators across all eight screens, we compiled a list of 150 genes containing genes recovered at FDR ≤ 5% in at least two independent substrate screens. Unbiased hierarchical clustering highlighted distinct categories of genes whose deletion either promoted or inhibited phagocytosis for all substrate types, or whose deletion had differential effects for different types of substrates. In general, genes known to participate in the same process clustered together (Fig. 1g).

We manually binned genes recovered at FDR ≤ 5% in at least three genome-wide screens into functional categories based on their reported roles within the cell (Fig. 2). Among the highest-confidence hits were the aforementioned members of the SCAR/WAVE and ARP2/3 complexes, all ten nonredundant members of which were hits for almost every substrate screened. The ARP2/3 complex has recently been shown to be of limited importance for IgG-mediated phagocytosis[40], and ARP2/3 components showed the lowest signal in IgGRBC screens (Fig. 2). Among the most prominent negative regulators of phagocytosis were seven genes associated with sialic acid biosynthesis and protein sialylation (Fig. 2). Genes related to surface signaling (such as the integrin-associated genes *ITGB2*, *TLN1* and *FERMT3*) and intracellular phosphorylation cascades (such as PP2A, MAPK and PKC-related genes) were among the hits with the strongest differential impact across different substrates.

Orthogonal validation of phagocytosis screen hits. Our magnet-based phagocytosis screens yielded hundreds of hits, however we

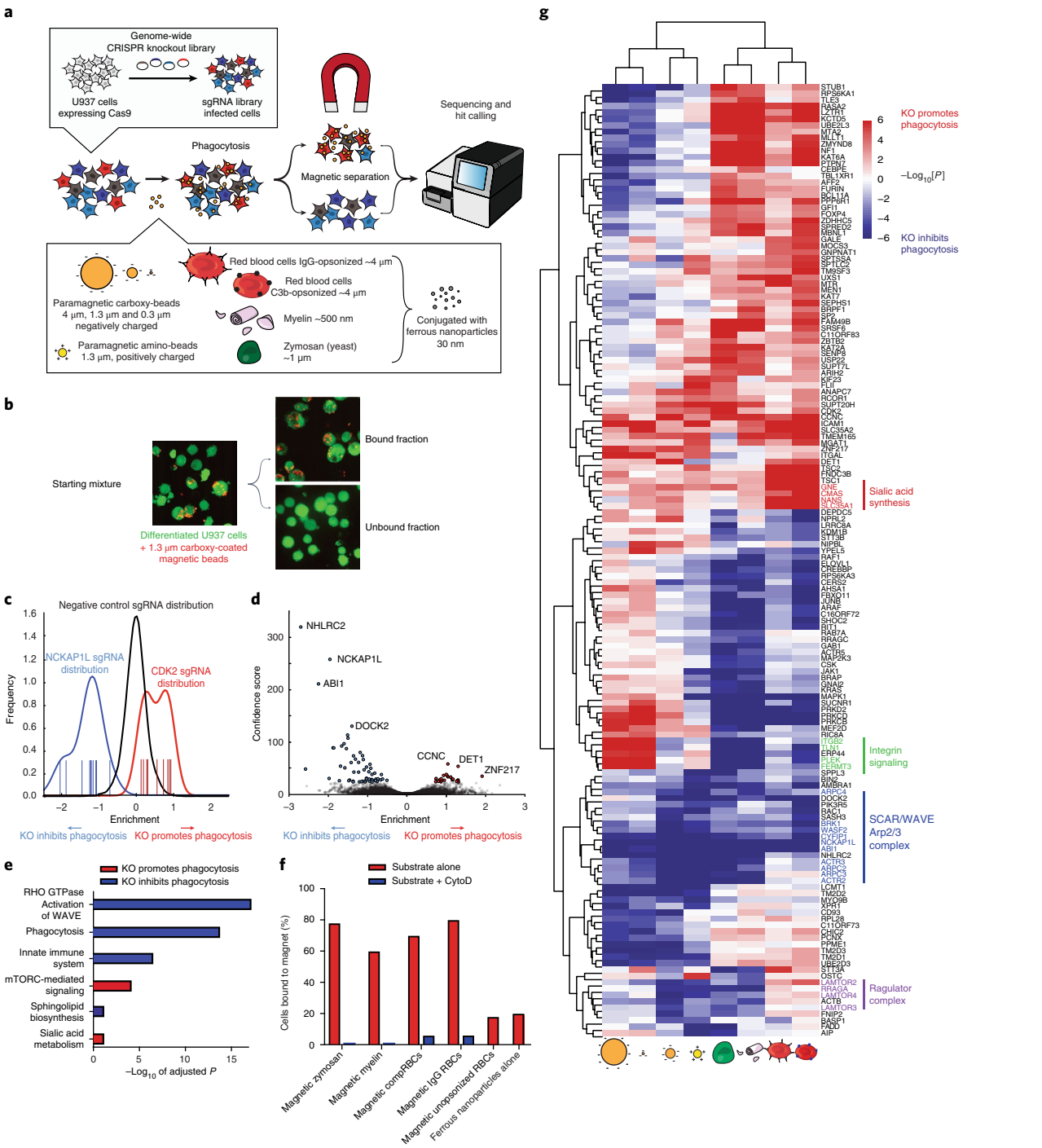

Fig. 1 | Genome-wide CRISPR screening for genetic regulators of phagocytosis. a, Schematic of phagocytosis screening strategy using magnetic separation. Labeling with ferrous nanoparticles enables magnetic separation screening of diverse substrates and comparison with paramagnetic beads of different size and charge. **b**, Confocal microscopy demonstrates efficient magnetic separation of phagocytosing and nonphagocytosing cells from a mixed population (1.3 μm magnetic beads). Representative of four independent experiments. **c**, sgRNA distributions for two example hits and the distribution of negative-control sgRNAs from a genome-wide phagocytosis screen using 1.3 μm magnetic beads. Positive values indicate enrichment in magnet-bound fraction, and negative values indicate enrichment in unbound fraction. Enrichment of ten sgRNAs targeting *NCKAP1L* and *CDK2*, blue and red vertical lines, respectively. Distribution of ~10,000 negative controls, black. KO, knockout. **d**, Volcano plot of all genes indicating effect and confidence scores for genome-wide phagocytosis screen using 1.3 μm magnetic beads. Effect and confidence scores determined by casTLE. The 85 genes passing 10% FDR for inhibiting or promoting phagocytosis are highlighted in blue and red, respectively. **e**, Select Reactome categories enriched in the 85 genes that pass the 10% FDR cutoff as determined by casTLE (Reactome category IDs listed in Methods; some categories are abbreviated). **f**, Phagocytosis of diverse substrates is actin dependent. Cells were pretreated with the actin polymerization inhibitor cytochalasin D (CytoD) before exposure to ferrous nanoparticle–labeled zymosan, myelin, C3b-opsonized RBCs (compRBCs), IgG-opsonized RBCs, or unopsonized RBCs. Binding to magnetic column was compared to untreated cells. **g**, Comparison of phagocytosis screen results with eight different substrates using unbiased hierarchical clustering, based on 150 genes that reached a FDR < 5% cutoff as determined by casTLE in at least three screens. Select, functionally related sets are highlighted.

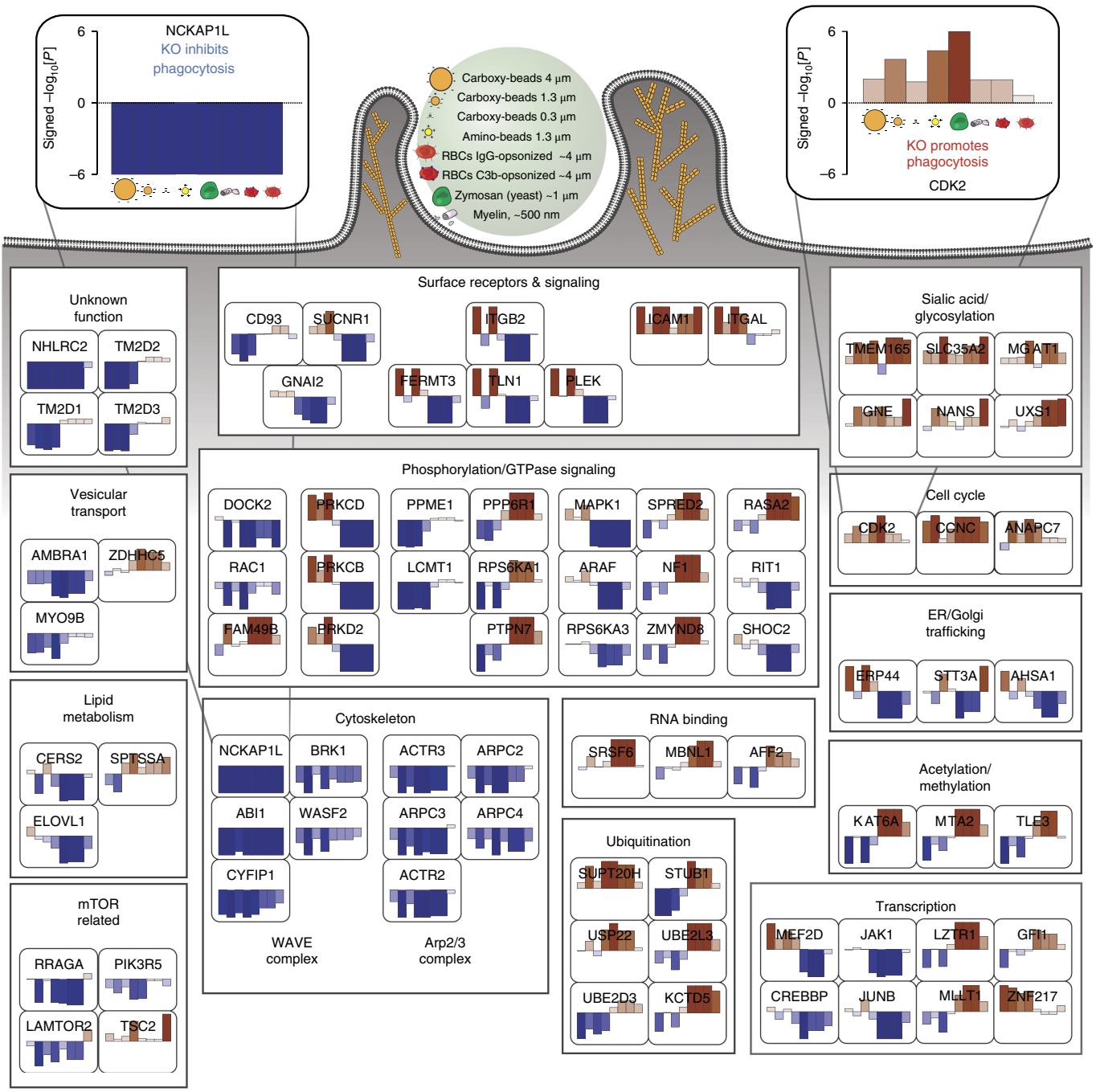

Fig. 2 | Putative modifiers of phagocytosis of diverse substrates from eight genome-wide screens. Bar plots represent signed $\log_{10}[P]$ for each gene for each substrate as calculated by casTLE using two replicate screens for each of eight different substrates. Each gene represented passed a 5% FDR threshold in at least three genome-wide phagocytosis screens. Negative values (blue bars) indicate that gene knockout inhibits phagocytosis, and positive values (red bars) indicate that gene knockout promotes phagocytosis. Annotations of cellular processes and compartments were based on literature and Gene Ontology (GO)-term assignments. ER, endoplasmic reticulum.

considered that some hits could result from properties unique to the magnetic separation process. To confirm that genes identified in these genome-wide screens were indeed related to phagocytosis, we performed an orthogonal FACS-based validation screen in which phagocytosis is monitored by the pH-sensitive fluorescent dye pHrodo (Fig. 3a). To do this, we generated a smaller sublibrary comprising sgRNAs targeting 322 genes identified as hits in the first BigBead and CompRBC genome-wide screens (Supplementary Tables 5 and 6). The reduced scale of the sublibrary enabled rapid FACS-based selection of 3×10^6 cells (~900× coverage). There was some agreement between the effect of sgRNAs in the FACS-based screen and the magnetic screens ($R^2=0.4$) (Fig. 3b), indicating that screen hits are not limited to idiosyncrasies of the magnetic selection method.

To further refine a high-confidence set of differential hits across diverse substrates, we again used our magnetic separation approach to screen the small sublibrary using six substrates at much higher coverage than in the genome-wide screens (60,000 cells per unique guide versus 1,000 cells per unique guide). This increased coverage, as determined by the number of cells per

unique guide, improves the sensitivity and robustness of large-scale screens[33,41]. In particular, for certain substrates the genome-wide screens exhibited low signal and high noise (Supplementary Fig. 3b), possibly due to the single magnetic separation step or heterogeneous differentiation and phagocytosis in U937 cells. Although the FDR can be controlled with stringent filtering, this may lead to many false negatives, that is, genes that affect phagocytosis but do not reach significance due to noise and/or small effect sizes. As we expected, the high-coverage sublibrary screens showed higher reproducibility between replicate screens (Supplementary Fig. 3c) and general agreement with genome-wide screens (Supplementary Fig. 4a,b), although certain screens showed some apparent false positive results. The batch retest screens showed phenotypes for many genes that had been missed in the genome-wide screens (false negatives). Additionally, we created a library targeting the 218 mouse genes whose human orthologs showed strong effects in the genome-wide midbead screen and screened it using FACS-based separation in one of the most widely studied phagocytic cell lines, mouse RAW 264.7 cells. Although this cross-species comparison in a different cell line identified many genes that seem to have species-specific or cell-type specific effects on phagocytosis, 81 of the genes in this library still demonstrated a significant phagocytosis phenotype (Supplementary Fig. 4b and Supplementary Table 5). Together, these focused, high-coverage sublibrary screens largely confirmed hits identified in genome-wide screens, and further supported the findings of strong effects for several poorly characterized genes (Supplementary Table 5).

Additionally, we generated 34 stable U937 cell lines expressing Cas9 and individual sgRNAs targeting hits identified at 10% FDR in our genome-wide screens, and confirmed high rates of gene editing (Supplementary Fig. 4g). We then measured rates of phagocytosis using automated time-lapse microscopy of pHrodo-labeled substrate. For example, differentiated U937 cells expressing sgRNAs against the SCAR/WAVE complex member *NCKAP1L* exhibited markedly reduced phagocytosis (Fig. 3c,d). These orthogonal time-lapse microscopy validation assays demonstrated varying degrees of reduced or increased phagocytic capacity across multiple substrates, largely mirroring the original screen results (Fig. 3e, Supplementary Fig. 4c,d and Supplementary Table 7) and validated contributions of genes with no previously reported role in phagocytosis (Fig. 3e). Together, about 70–80% of genes (depending on substrate) measured in these individual assays exhibited a phenotype consistent with their phenotype in the pooled screens. Finally, we validated the roles of select genes by CRISPR editing in primary human macrophages isolated from peripheral blood, suggesting that hits discovered in these screens are not limited to immortalized cell lines (Figs. 3f,5e and 6f and Supplementary Fig. 4i).

Identifying substrate-selective phagocytosis regulators. Notably, the screens identified several genes whose disruption had a differential impact on phagocytosis for certain substrates. To directly test the effect of these genes on substrate preference, we adapted our live-imaging phagocytosis assay to simultaneously monitor uptake of two separate particles labeled with pHrodo red and pHrodo green, respectively (Fig. 3g). Using this approach, we challenged several sgRNA-expressing U937 cell lines either with a mixture of red zymosan and green positive midbeads or with a mixture of red CompRBC and green positive midbeads. Consistent with the screen results, U937 cells expressing sgRNAs against integrin-related genes *TLN1* and *FERMT3* showed marked reduction in phagocytosis of zymosan and CompRBC, whereas their ability to phagocytose beads remained intact (Fig. 3h–j). Additionally, we confirmed that *PLEK*, which coordinates actin polymerization and is enriched at the phagocytic cup[42,43], also contributes to uptake of zymosan and complement-opsonized red blood cells, but not beads (Fig. 3h–j).

Multiple magnetic screens predicted that knockout of *PLEK*, *TLN1*, *ICAM1* and *CDK2* would boost bead phagocytosis. Notably, whereas cell lines expressing *CDK2* sgRNAs similarly increased uptake of beads measured using pHrodo-labeled beads (which measure pH drop upon phagosome fusion to the lysosome) (Supplementary Fig. 4d), there was no increase in phagocytosis in pHrodo-based assays for *ICAM1*, *PLEK* or *TLN1* knockouts (Fig. 3h–j and Supplementary Fig. 4d). To investigate this discrepancy, we tested cells carrying sgRNAs for *PLEK* or *TLN1* in magnetic separation assays after exposure to magnetized zymosan or magnetic beads. Indeed, these assays again confirmed deficits in zymosan uptake for these lines and showed increased capture of bead-exposed cells (Supplementary Fig. 4f). U937 cells carrying *ICAM1* sgRNAs similarly showed no effect in pHrodo-based assays, but showed increased magnetic capture after phagocytosis of magnetic beads or zymosan (Supplementary Fig. 4e). Thus, although the assays are largely well correlated (Fig. 3b), certain phagocytosis regulators we identified showed selective effects in magnetic bead uptake versus pHrodo bead uptake assays; this could reflect action at distinct steps of phagocytosis. This underscores the value of using orthogonal assays to probe the activity of identified phagocytosis regulators.

Discovery of an essential role for NHLRC2 in phagocytosis. A particularly conspicuous hit from our screening data sets was *NHLRC2*, a poorly characterized gene that was reproducibly one of the strongest hits required for phagocytosis in almost every screen. To further validate the role of NHLRC2 during phagocytosis, we examined its function in RAW 264.7 cells. RAW 264.7 cell lines were generated that constitutively expressed Cas9 and an sgRNA targeting either *NHLRC2* or the SCAR/WAVE component *NCKAP1L*. We observed almost identically strong defects in phagocytosis for two independent sgRNAs targeting each of these genes (Supplementary Fig. 5a). To further validate this observation, we generated clonal *NHLRC2* knockout RAW 264.7 and U937 cells, confirmed them by Sanger sequencing (Supplementary Fig. 4h) and found severe phagocytosis deficits. (Fig. 4a,b and Supplementary Fig. 5b). We also validated the inhibitory effect on phagocytosis when knocking out these genes in primary human macrophages (Fig. 3f).

To investigate the molecular function of NHLRC2, we performed BioID pulldown experiments[44] using a mutant form of the biotin ligase enzyme BirA (BirA*) fused to NHLRC2 in order to make a BirA*-NHLRC2 fusion protein. This approach allows for the unbiased assessment of transient or stable NHLRC2 interactions within the native cellular environment of differentiated U937 cells. BirA*-NHLRC2 pulldown samples were highly enriched for several transmembrane and perimembrane proteins in addition to NHLRC2 itself (Fig. 4c and Supplementary Table 8). To our surprise, none of the partners were identified as a hit in any of our phagocytosis screens, possibly due to redundancy of NHLRC2-associated proteins (see Discussion). However, gene ontology and Kyoto encyclopedia of genes and genomes (KEGG) enrichment analysis of pulldown hit genes identified enrichment in annotated phagocytosis regulators (Supplementary Table 8), with two candidates (LSP1 and p190RhoGAP) directly implicated in directing actin polymerization at the cell surface[45,46]. Therefore, we hypothesized that *NHLRC2* contributes to phagocytosis by assisting LSP1 or p190RhoGAP coordination of actin polymerization.

p190RhoGAP (also known as GRLF1 or ARHGAP35) is a negative regulator of RHOA and localizes to the phagocytic cup[47]. RHOA influences bundled actin dynamics and antagonizes Rac1-mediated rearrangements of branched cortical actin. We therefore tested whether loss of *Nhlrc2* alters RHOA or RAC1 activation. *Nhlrc2* knockout RAW 264.7 cells showed substantially elevated levels of RHOA activation specifically during phagocytosis, although global levels of RAC1 activation were minimally altered in total cell

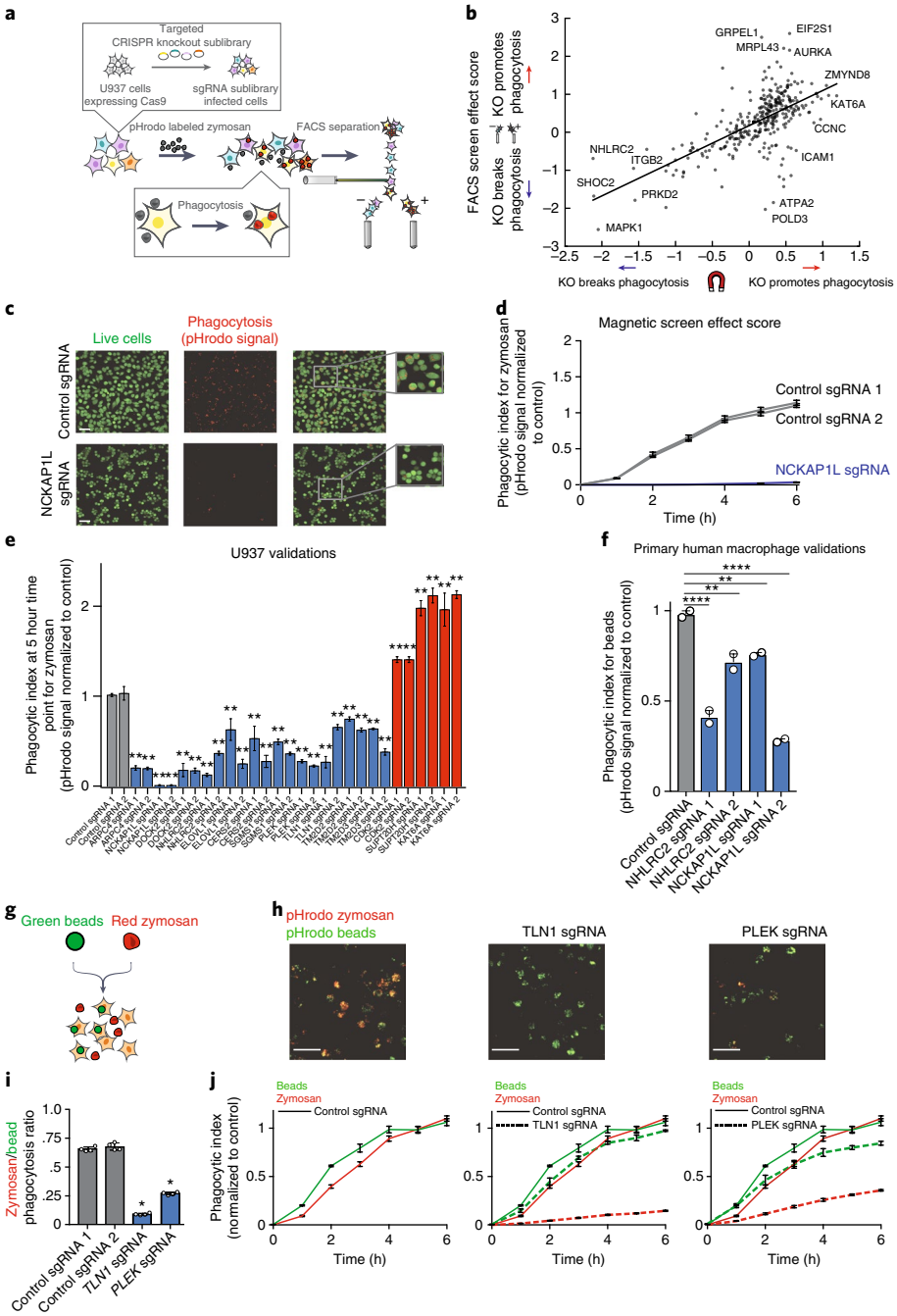

Fig. 3 | Orthogonal measurements of phagocytosis validate magnetic screen results. a, Design of FACS-based validation screen. Differentiated U937 cells containing a custom sgRNA library targeting 322 genes identified in genome-wide screens were FACS sorted based on fluorescence signal from pHrodo-labeled zymosan. **b**, Correlation of casTLE effect scores between FACS and magnetic separation screens using the 322-gene custom sgRNA library. **c**, U937 cells expressing a *NCKAP1L* sgRNA treated with pHrodo-labeled zymosan (red). Live cells were labeled with calcein AM (green). Representative of six independent experiments. Scale bars, 50 µm. **d**, Automated live cell microscopy was used to monitor signal from pHrodo zymosan over time. A phagocytic index was calculated by measuring the total area of pHrodo signal divided by the total live cell area, then normalized to the average value of the control lines at 5 h. Values represent mean ± s.e.m. of $n = 4$ replicate wells. **e**, Summary of additional validations. The phagocytic index at 5 h is presented. Values represent mean ± s.e.m. of $n = 4$ replicate wells. (**$P < 0.01$, *$P < 0.05$, two-way analysis of variance (ANOVA) with Dunnett's comparison to control sgRNA). **f**, Validation in primary human macrophages. FACS measurement of pHrodo-labeled bead phagocytosis with either control sgRNA or sgRNAs targeting *NCKAP1L* or *NHLRC2*. Results are normalized to the maximal response by each independent donor. Values represent mean ± s.e.m. of $n = 4$ (*NHLRC2* or *NCKAP1L*) or $n = 6$ (control) technical replicates. Dots represent averaged technical replicates across $n = 2$ biological donors. **$P < 0.01$, ****$P < 0.0001$ (one-way ANOVA with multiple-comparisons correction). **g**, Schematic for competitive phagocytosis assay to validate substrate specific regulators of phagocytosis. **h**, Example images from competitive phagocytosis assays of zymosan (red) and 1.3 µm beads (green) in U937 cells expressing a control sgRNA, *TLN1* sgRNA or *PLEK* sgRNA. Images are representative of two independent experiments. Scale bars, 10 µm. **i**, Ratio of total red area (zymosan) to total green area (bead) at 5 h in cells expressing control sgRNA or sgRNAs targeting *TLN1* or *PLEK*. Values represent mean ± s.e.m. *$P < 0.05$, two-tailed *t*-test from $n = 4$ technical replicates; results are representative of three independent experiments. **j**, Phagocytic index of zymosan (red) and beads (green) in competitive phagocytosis assay over time. Values represent mean ± s.e.m. of $n = 4$ replicate wells; results are representative of three independent experiments.

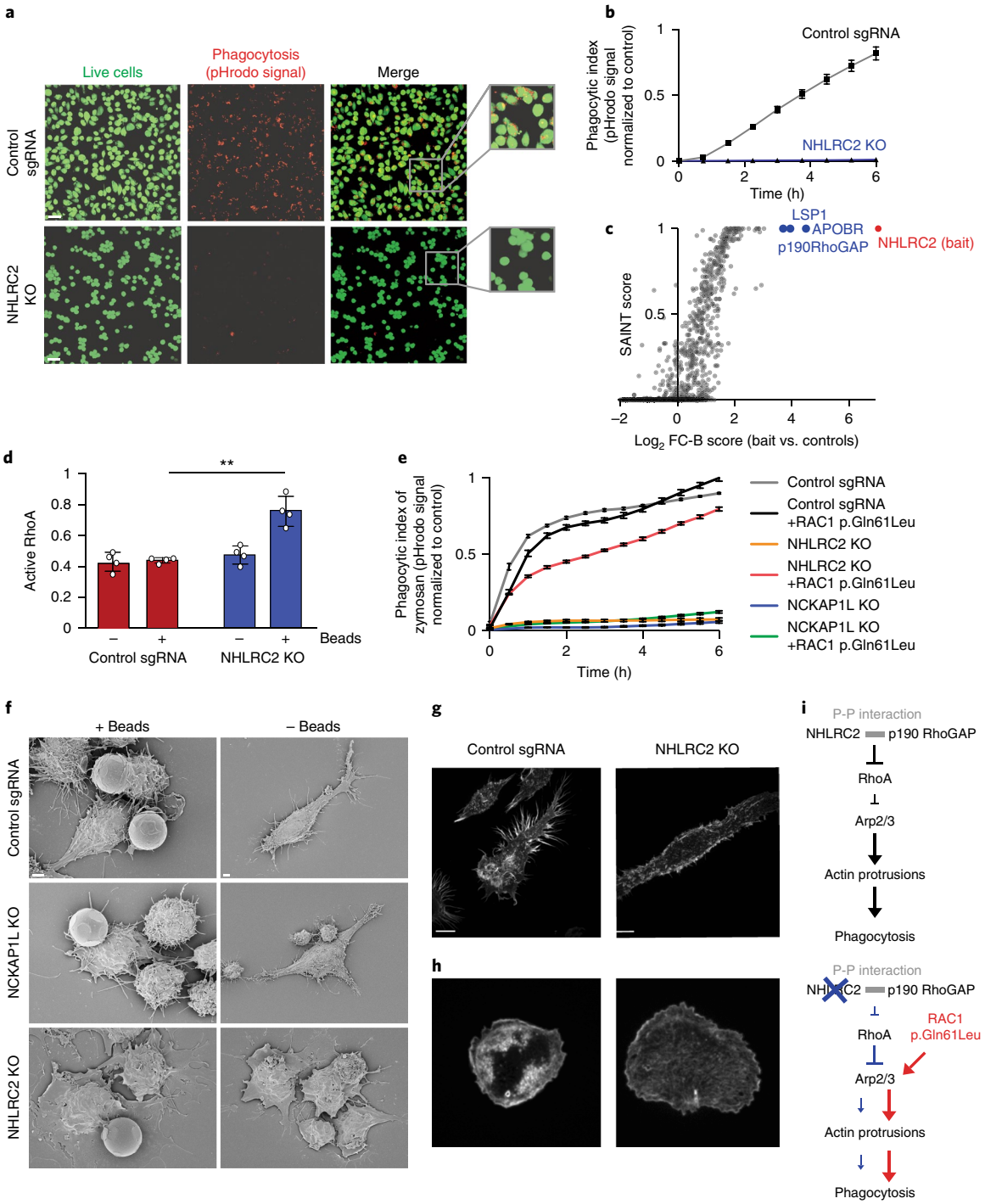

Fig. 4 | Loss of NHLRC2 inhibits phagocytosis through Rho/Rac1 signaling. a, Clonally derived U937 cells with verified *NHLRC2* knockout were labeled with calcein AM (green) after 5 h of exposure to pHrodo-labeled zymosan (red). Representative of six independent experiments. Scale bar, 50 µm. **b**, Phagocytic index (see Fig. 3) of pHrodo-labeled zymosan from control sgRNA-expressing U937s and clonally derived *NHLRC2* knockout (KO) U937 cells. Values represent mean ± s.e.m. of $n = 4$ replicate wells. **c** Results from BioID for NHLRC2. Enrichment of a protein in the NHLRC2-BirA pulldown versus BirA alone is plotted against the mean confidence score (SAINT score) ($n = 3$ experimental replicates). The bait protein (NHLRC2) is highlighted in red and top protein interactors are highlighted in blue. **d**, Quantification of active (GTP-bound) RhoA in RAW 264.7 cells expressing a control sgRNA (red) or confirmed *Nhlrc2* KO RAW 264.7 cells (blue) as determined by ELISA. Signal was normalized against recombinant GTP-bound RhoA. Values represent mean ± s.e.m. of $n = 3$ experimental replicates (**$P < 0.005$, two-tailed *t*-test). **e**, Phagocytic index measurements using pHrodo-labeled zymosan of RAW 264.7 cells expressing a control sgRNA (grey) with constitutively active (CA) RAC1 (black), *Nhlrc2* KO cell line (yellow) with CA RAC1 (red), *Nckap1l* KO cell line (blue) with CA RAC1 (green). Values represent mean ± s.e.m. for $n = 4$ replicate wells. **f**, SEM of RAW 264.7 cells with control sgRNA (top row), *Nckap1l* KO (middle row) and *Nhlrc2* KO (bottom row) with (left) and without beads (right). Representative images of three experimental replicates. Scale bar, 2 µm. **g**, F-actin staining (AlexaFluor 488 phalloidin) of RAW 264.7 with control sgRNA (left) and *Nhlrc2* KO (right). Representative images of three experimental replicates. Scale bars, 10 µm. **h**, F-actin staining of control sgRNA (left) and *Nhlrc2* KO (right) RAW 264.7 cells engaging IgG-coated coverslips during frustrated phagocytosis. Scale bars, 10 µm. **i**, Model for role of NHLRC2 in phagocytosis. P-P interaction, protein-protein interaction.

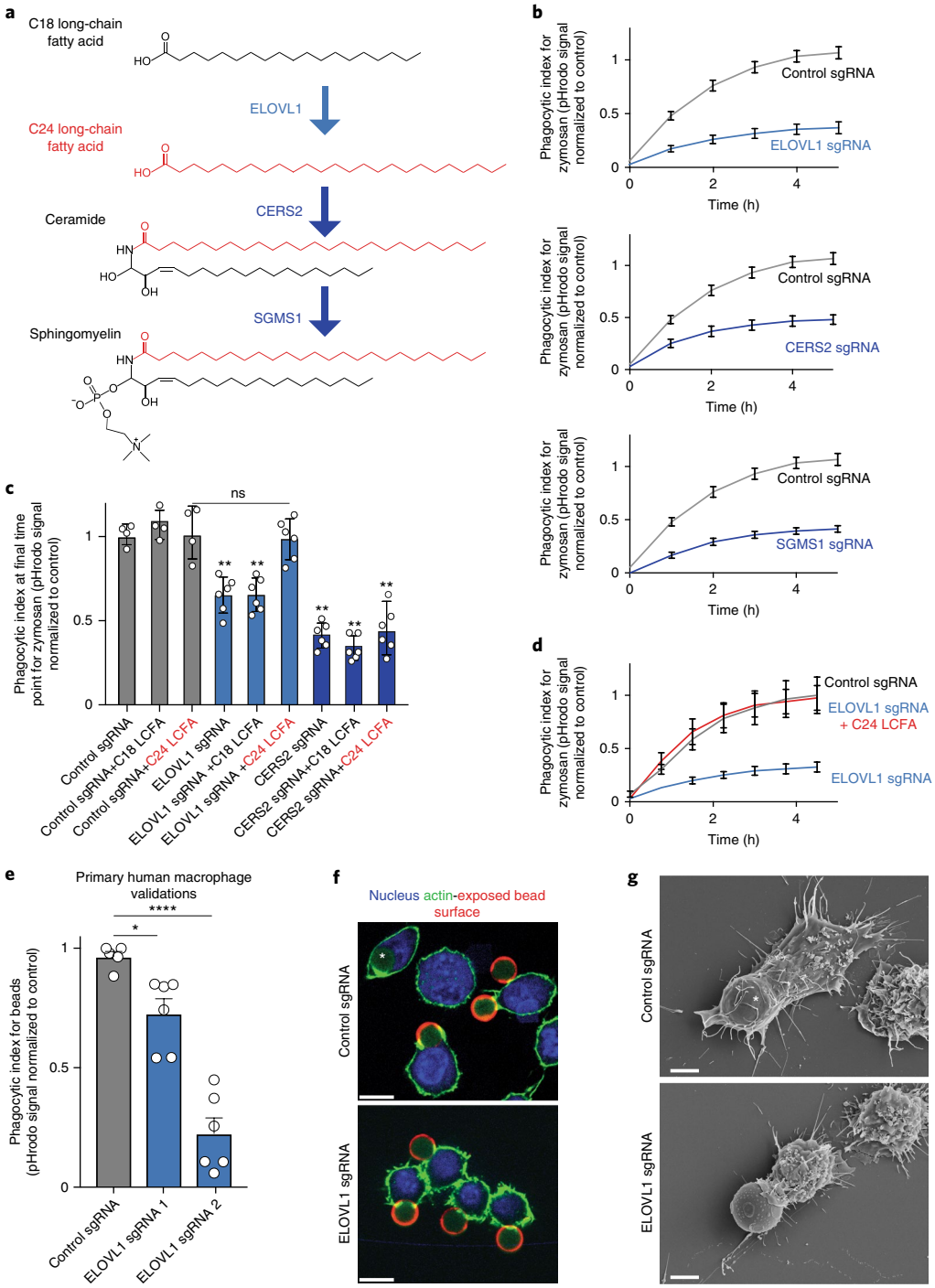

Fig. 5 | Role for VLCFAs in phagocytosis. a, Genes identified in the genome-wide screens as required for phagocytosis (*ELOVL1*, *CERS2* and *SGMS1*) participate in consecutive steps of a lipid biosynthetic pathway. **b**, Validation of pathway members using automated microscopy. Phagocytosis was monitored over time as in Fig. 3 using U937 cells containing the indicated guide and pHrodo-labeled zymosan. Values represent mean ± s.e.m., $n = 6$ replicate wells. **c**, Rescue of ELOVL1 deficiency by long-chain fatty acid (LCFA) supplementation. Phagocytosis measured at 5 h from U937 cells expressing control (grey), *ELOVL1* (light blue) or *CERS2* sgRNA (dark blue) supplemented with C18 or C24 LCFAs. Values represent mean ± s.e.m., $n = 6$ replicate wells. (**$P < 0.01$, one-way ANOVA with Dunnett's comparison to control sgRNA). **d**, Phagocytic index over time for U937 lines expressing control sgRNA (grey), *ELOVL1* sgRNA (blue) or *ELOVL1* sgRNA and supplemented with C24 LCFA (red). Values represent mean ± s.e.m., $n = 4$ replicate wells. **e**, Validation of *ELOVL1* phagocytic function in primary human macrophages. FACS measurement of pHrodo-labeled zymosan phagocytosis by macrophages electroporated with either control sgRNA or sgRNAs targeting *ELOVL1*. Results normalized to the maximal response by each independent donor. Values represent mean ± s.e.m. of $n = 5$ (control or sgRNA 2) or $n = 6$ (sgRNA 1) technical replicates. Experiments performed with $n = 3$ biological donors. Dots represent technical replicates. *$P < 0.05$, ****$P < 0.0001$ (one-way ANOVA with multiple-comparisons correction). **f**, RAW 264.7 cells expressing control sgRNA (top) or *ELOVL1*-targeting sgRNA (bottom) were incubated with IgG-coated 7 µm beads for 10 min and fixed. IgG signal (red) marks bead surfaces unobstructed by cellular contact. Cells were stained with phalloidin (green) and Hoechst nuclear stain (blue). White asterisk marks a fully internalized bead. Representative of two independent experiments. Scale bars, 10 µm. **g**, SEM of RAW 264.7 cells expressing control sgRNA (top) or *ELOVL1* sgRNA (bottom) that were incubated with IgG-coated 7 µm beads for 10 min and fixed. White asterisk marks a fully internalized bead.

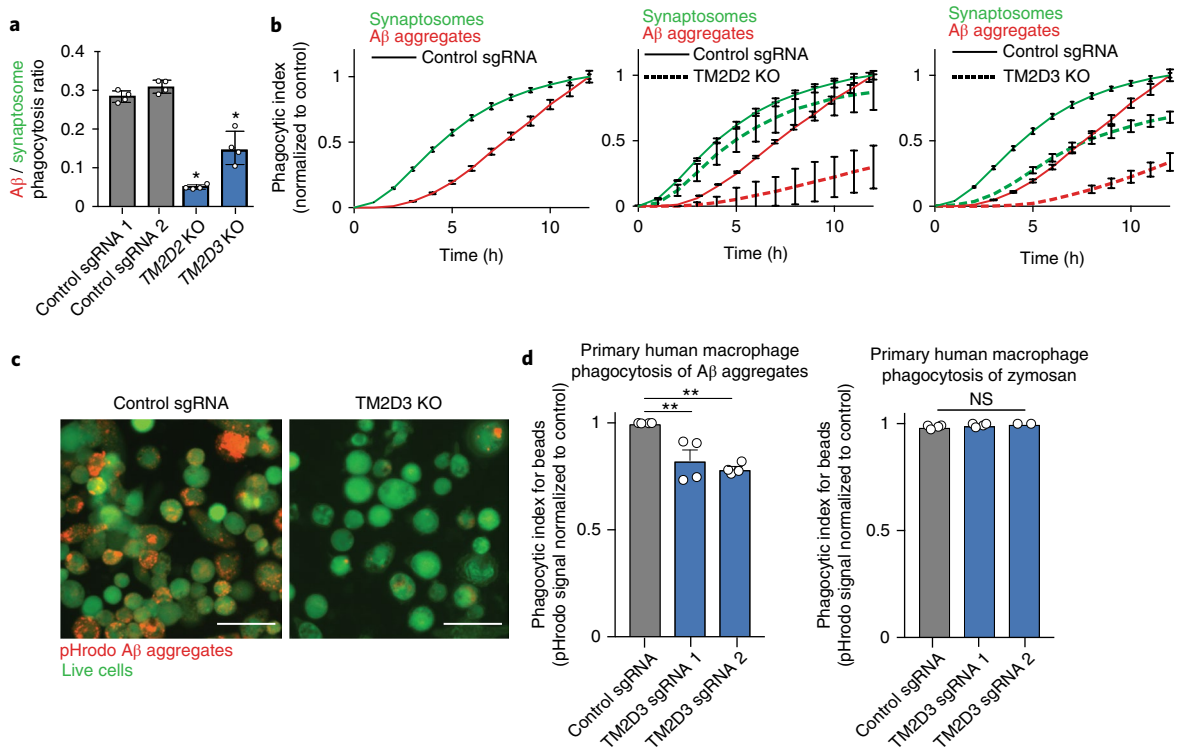

Fig. 6 | Identification of substrate specific regulators of phagocytosis. a, Ratio of total red area (indicating phagocytosis of amyloid-β (Aβ) aggregates) to total green area (indicating phagocytosis of synaptosomes) at final time point of phagocytosis assay in cells expressing control sgRNA or confirmed U937 *TM2D3* and *TM2D2* clonal knockout lines. Values represent mean ± s.e.m. of $n = 4$ replicate wells (*$P < 0.05$, two-tailed *t*-test). **b**, Competitive phagocytosis assay in U937 cells expressing control sgRNAs or confirmed U937 *TM2D3* and *TM2D2* clonal knockout lines. Synaptosomes are labeled with pHrodo green and amyloid-β aggregates with pHrodo red. Phagocytic index for each substrate measured over time using automated live cell imaging. Values represent mean ± s.e.m. of $n = 4$ replicate wells (*$P < 0.05$, two-tailed *t* test). **c**, Phagocytosis of amyloid-β aggregates (labeled with pHrodo red) is impaired in confirmed clonal U937 *TM2D3* knockout line when compared to U937s expressing control sgRNA. Live U937 cells labeled with calcein AM (green). Representative of three independent experiments. Scale bar, 10 μm. **d**, Validation in primary human macrophages of role of TM2D3 in amyloid-β aggregates and zymosan phagocytosis. Flow cytometry-based measurement of phagocytosis of pHrodo-labeled amyloid-β aggregates or of pHrodo-labeled zymosan by genetically modified macrophages electroporated with either control sgRNA or sgRNAs targeting *TM2D3*. Results normalized to maximal response by each independent donor. Values represent mean ± s.e.m. of $n = 2$–4 technical replicates. Experiments performed with $n = 2$ biological donors. Dots represent technical replicates. **$P < 0.01$ (one-way ANOVA with multiple-comparisons correction).

lysates (Fig. 4d and Supplementary Fig. 5c). We next tested whether enhanced Rac1 activity could overcome *Nhlrc2* knockout phagocytic deficits by overexpressing a constitutively active Rac1 mutant (RAC1 p.Gln61Leu). RAC1 p.Gln61Leu overexpression rescued the phagocytic defect of *Nhlrc2* knockout cells without affecting control or *Nckap1l* knockout cells, supporting a model in which NHLRC2 is required for cytoskeletal rearrangements downstream of particle binding and receptor engagement (Fig. 4e). Closer examination of cellular morphology by scanning electron microscopy (SEM) revealed a marked loss of surface filopodia specific to *Nhlrc2* knockout cells relative to wild-type or *Nckap1l* knockout cells (Fig. 4f and Supplementary Fig. 5e), supporting a role for NHLRC2 in regulation of actin protrusions. We observed the absence of filopodia in *Nhlrc2* knockout cells using confocal microscopy after phalloidin staining to label F-actin (Fig. 4g and Supplementary Fig. 5d) as well as the failure of these cells to form organized actin structures in a frustrated phagocytosis assay (Fig. 4h and Supplementary Videos 1 and 2). Together, these data suggest a model in which NHLRC2 negatively regulates RHOA, enabling RAC1-mediated cytoskeletal changes that are critical for phagocytosis (Fig. 4i).

VLCFAs are necessary for efficient phagocytosis. Some of the unexpected screen hits were members of a sequential lipid biosynthesis pathway (Fig. 5a). These included a fatty-acid elongase that generates very-long-chain fatty acids (VLCFAs) (*ELOVL1*), and a ceramide synthase that specifically incorporates VLCFAs into ceramides (*CERS2*); both were strong hits for multiple substrates (Fig. 1g). A downstream sphingomyelin synthase that adds a zwitterionic head group to a diverse range of ceramides (*SGMS1*)[48] was also a hit, though with weaker and more variable effects. In validation experiments, sgRNAs targeting any of these three enzymes strongly reduced phagocytosis of zymosan (Fig. 5b). To test whether the contribution of these genes to phagocytosis is solely related to the presence of these lipid species, we performed metabolic rescue experiments. Phagocytosis deficiency of cells with disrupted *ELOVL1* function was rescued by supplementation with its product VLCFAs (a mixture of C24:0 and C24:1) but not with its substrate medium-chain fatty acids (a mixture of C18:0 and C18:1, Fig. 5c,d). Importantly, control cells were not affected and cells carrying an sgRNA against the downstream enzyme *CERS2* were not rescued. We further validated the role of *ELOVL1* in phagocytosis by CRISPR editing in primary human macrophages; despite incomplete gene editing (Supplementary Fig. 4i), we observed a significant decrease in phagocytosis upon *ELOVL1* gene disruption (Fig. 5e).

Notably, confocal microscopy of *ELOVL1* knockout RAW 264.7 cells incubated with IgG-coated 7 μM beads and fixed after 10 min indicated that a majority of phagocytic cups are stalled at early cup formation. In contrast, we observed all steps of phagocytic cup

formation, including fully engulfed beads, in control cells (Fig. 5f, Supplementary Fig. 6a and Supplementary Videos 3,4). The phenotype of early phagocytic cup stalling in *ELOVL1* knockout cells was also observed with SEM (Fig. 5g and Supplementary Fig. 6b).

Because the process of cell migration involves similar actin dynamics and many of the same molecular components as phagocytosis, we tested whether VLCFAs might have a role in migration. Notably, knockdown of *ELOVL1* in a human neutrophil cell line (PLB-985) reduced basal cell migration speed, although not as strongly as knockdown of positive-control genes (*ACTR2* and *RAC2*, which have roles in both phagocytosis and cell motility[49] (Supplementary Fig. 6c). This motility defect was reduced after stimulation with a formyl peptide chemoattractant (Supplementary Fig. 6d). For the two sgRNAs we tested, the strength of the knockdown was correlated with the strength of the phenotype (Supplementary Fig. 6c–e). Taken together, our results suggest a previously unappreciated role of these specific VLCFAs in basic immune cell functions requiring large morphological transitions such as macrophage phagocytosis and neutrophil motility.

Alzheimer's risk gene *TM2D3* controls amyloid-β uptake. In addition to the integrin-related genes we identified as specifically affecting uptake of a subset of particles (Supplementary Fig. 7a,b), we chose to focus on the TM2D family (*TM2D1*, *TM2D2* and *TM2D3*), several components of which were consistently recovered as hits required for phagocytosis for various bead types but were either not hits or had weak effects on uptake of most biological particles (Figs. 1g and 2).

TM2D1 has been implicated in binding to amyloid-β peptide[50], and a *TM2D3* variant allele has been recently identified as strong risk factor for late-onset Alzheimer's disease, with an odds ratio of 3.5–15.9 (ref. [51]). Therefore, we hypothesized that TM2D family members participate in engulfment of amyloid-β protein aggregates. To test this proposal, we generated small pHrodo-conjugated amyloid-β aggregates according to described protocols[52]. Control cells showed actin-dependent accumulation of pHrodo signal, and uptake was abolished with the addition of cytochalasin D (Supplementary Fig. 7c). Uptake of pHrodo-conjugated amyloid-β aggregates was also markedly reduced in U937 cells with sgRNAs targeting universally required phagocytosis regulators, such as *NCKAP1L* and *NHLRC2* (Supplementary Fig. 7c). Because phagocytosis of both amyloid-β aggregates and synaptic material are thought to be important for Alzheimer's disease progression[4] and our screens predicted strong substrate-specific contributions of TM2D family members, we next tested whether knockout lines could discriminate between simultaneously applied pHrodo-red amyloid-β and pHrodo-green synaptosomes. *TM2D2* and *TM2D3* knockout lines showed substantial deficiencies in amyloid-β phagocytosis, but less of a change in clearance of synaptic material in a competition assay (Fig. 6a–c), highlighting the potential significance of central nervous system (CNS) substrate–specific contributions of TM2D family proteins to the balance of phagocytosis in Alzheimer's disease. To further confirm the role of TM2D family proteins, we tested the role of *TM2D3* in the phagocytosis of amyloid-β aggregates and zymosan in primary human macrophages. Electroporation with Cas9 ribonucleoprotein complexes targeting *TM2D3* inhibited the phagocytosis of amyloid-β aggregates by peripheral blood monocyte–derived macrophages, but no change was detected for zymosan phagocytosis (Fig. 6d). Together, these data suggest that loss of *TM2D3* function may impair clearance of amyloid-β aggregates and related particles, with more limited impact on phagocytosis of other substrates.

Discussion

Here, we developed a rapid and efficient strategy to identify genes that control diverse aspects of phagocytosis using magnetic separation. We have implicated many known and uncharacterized genes as positive or negative regulators of phagocytosis, and validated the roles of dozens of individual genes using orthogonal assays. Together, our data illuminate both universal and substrate-specific principles of phagocytosis and identify multiple novel and poorly characterized genes that are central to phagocytic processes.

NHLRC2, one of the strongest hits across almost all of our screens, has been poorly characterized but is broadly expressed at relatively low levels in many cell types[53]. During preparation of this manuscript, mutations in *NHLRC2* were found to be associated with fatal fibrosis, CNS vascular abnormalities, and neurodegeneration in humans[54], and a role was proposed for *NHLRC2* in protection from cell death induced by reactive oxygen species[55]. Our results show that knockout of *NHLRC2* in U937 and RAW 264.7 cells profoundly inhibits phagocytosis of several types of substrates. Rescue of murine *Nhlrc2* knockout cells with constitutively active Rac1 suggests that phagocytic signaling can be restored and that cells lacking NHLRC2 protein are otherwise capable of executing the steps required for phagocytosis. With the additional observation that NHLRC2 associates with p190RhoGAP and alters activation of the cytoskeleton regulator RHOA, we propose a model in which NHLRC2 helps to initiate localized RHOA inhibition, enabling RAC1-driven cytoskeletal rearrangement during initiation of phagocytosis. The mechanism by which loss of NHLRC2 results in loss of filopodia (Fig. 4f,g) will require further investigation, but may partially explain the profound defect in phagocytosis observed in these mutant cells[56].

We found clusters of genes with differential effects on distinct substrates; for example, integrin signaling is required for uptake of several biological particles but not charged beads (Figs. 1g and 2). Integrins can act as phagocytic receptors themselves, but they also facilitate initiation of phagocytic signaling cascades after engagement of other surface receptors. Additionally, we found that PLEK, which serves to localize and initiate signaling cascades that direct cytoskeletal rearrangements and can be localized to the phagocytic cup[42,43], has a role only upon engagement of certain substrates. Conversely, many genes regulate phagocytosis of beads but not biological particles (Fig. 1g). Further studies will be necessary to investigate the mechanisms that account for these differences.

In considering hits with disproportionate impacts on different particle types, we were particularly intrigued by the TM2-domain family members because they are poorly characterized and have been implicated in neurodegenerative disease. We found that *TM2D2*- and *TM2D3*-deficient cells show impaired clearance of amyloid-β aggregates, and that the phagocytic defect had a disproportionate effect on protein aggregates relative to another CNS-relevant substrate. Previous findings that TM2D1 can directly bind to amyloid-β peptide[50] suggests that these genes may contribute to initial events required for aggregate uptake. However, all three TM2-domain family members are broadly expressed by diverse cell types[53], and they may have a more general role in cellular signaling events related to disease progression.

The ability to rapidly screen for phagocytosis regulators at the genome scale makes it possible to investigate how phagocytosis machinery changes across cellular activation states or in diverse environmental conditions. Further optimization could address limitations of this approach and should allow more detailed dissection of particular steps of phagocytic particle engulfment (see Supplementary Note). Together, this work establishes a broadly applicable strategy for investigating complex cellular uptake processes and promises to yield insights into diseases characterized by dysregulated phagocytosis.

URLs. EnrichR, http://amp.pharm.mssm.edu/Enrichr; casTLE, https://bitbucket.org/dmorgens/castle; ICE Analysis Tool, https://ice.synthego.com; the Galaxy platform, https://usegalaxy.org/; SAINT analysis, https://reprint-apms.org/.

Online content

Any methods, additional references, Nature Research reporting summaries, source data, statements of data availability and associated accession codes are available at https://doi.org/10.1038/s41588-018-0254-1.

Received: 29 June 2018; Accepted: 11 September 2018;
Published online: 5 November 2018

References

1. Lim, J. J., Grinstein, S. & Roth, Z. Diversity and versatility of phagocytosis: roles in innate immunity, tissue remodeling, and homeostasis. *Front. Cell. Infect. Microbiol.* **7**, 191 (2017).
2. Gordon, S. Phagocytosis: an immunobiologic process. *Immunity* **44**, 463–475 (2016).
3. Arandjelovic, S. & Ravichandran, K. S. Phagocytosis of apoptotic cells in homeostasis. *Nat. Immunol.* **16**, 907–917 (2015).
4. Hong, S., Dissing-Olesen, L. & Stevens, B. New insights on the role of microglia in synaptic pruning in health and disease. *Curr. Opin. Neurobiol.* **36**, 128–134 (2016).
5. Vargas, M. E. & Barres, B. A. Why is Wallerian degeneration in the CNS so slow? *Annu. Rev. Neurosci.* **30**, 153–179 (2007).
6. Chao, M. P. et al. Anti-CD47 antibody synergizes with rituximab to promote phagocytosis and eradicate non-Hodgkin lymphoma. *Cell* **142**, 699–713 (2010).
7. Chen, J. et al. SLAMF7 is critical for phagocytosis of haematopoietic tumour cells via Mac-1 integrin. *Nature* **544**, 493–497 (2017).
8. Ziegenfuss, J. S., Doherty, J. & Freeman, M. R. Distinct molecular pathways mediate glial activation and engulfment of axonal debris after axotomy. *Nat. Neurosci.* **15**, 979–987 (2012).
9. Juncadella, I. J. et al. Apoptotic cell clearance by bronchial epithelial cells critically influences airway inflammation. *Nature* **493**, 547–551 (2013).
10. Chung, W. S. et al. Astrocytes mediate synapse elimination through MEGF10 and MERTK pathways. *Nature* **504**, 394–400 (2013).
11. Freeman, S. A. & Grinstein, S. Phagocytosis: receptors, signal integration, and the cytoskeleton. *Immunol. Rev.* **262**, 193–215 (2014).
12. Diakonova, M., Bokoch, G. & Swanson, J. A. Dynamics of cytoskeletal proteins during Fcgamma receptor-mediated phagocytosis in macrophages. *Mol. Biol. Cell* **13**, 402–411 (2002).
13. Fairn, G. D. & Grinstein, S. How nascent phagosomes mature to become phagolysosomes. *Trends Immunol.* **33**, 397–405 (2012).
14. Swanson, J. A. Shaping cups into phagosomes and macropinosomes. *Nat. Rev. Mol. Cell Biol.* **9**, 639–649 (2008).
15. Hedgecock, E. M., Sulston, J. E. & Thomson, J. N. Mutations affecting programmed cell deaths in the nematode *Caenorhabditis elegans*. *Science* **220**, 1277–1279 (1983).
16. Ellis, R. E., Jacobson, D. M. & Horvitz, H. R. Genes required for the engulfment of cell corpses during programmed cell death in *Caenorhabditis elegans*. *Genetics* **129**, 79–94 (1991).
17. Gumienny, T. L. et al. CED-12/ELMO, a novel member of the CrkII/Dock180/Rac pathway, is required for phagocytosis and cell migration. *Cell* **107**, 27–41 (2001).
18. Tosello-Trampont, A. C., Brugnera, E. & Ravichandran, K. S. Evidence for a conserved role for CRKII and Rac in engulfment of apoptotic cells. *J. Biol. Chem.* **276**, 13797–13802 (2001).
19. Logan, M. A. et al. Negative regulation of glial engulfment activity by Draper terminates glial responses to axon injury. *Nat. Neurosci.* **15**, 722–730 (2012).
20. Silva, E., Au-Yeung, H. W., Van Goethem, E., Burden, J. & Franc, N. C. Requirement for a *Drosophila* E3-ubiquitin ligase in phagocytosis of apoptotic cells. *Immunity* **27**, 585–596 (2007).
21. Garver, L. S., Wu, J. & Wu, L. P. The peptidoglycan recognition protein PGRP-SC1a is essential for Toll signaling and phagocytosis of *Staphylococcus aureus* in *Drosophila*. *Proc. Natl Acad. Sci. USA* **103**, 660–665 (2006).
22. Shen, K., Sidik, H. & Talbot, W. S. The Rag-Ragulator complex regulates lysosome function and phagocytic flux in microglia. *Cell Rep.* **14**, 547–559 (2016).
23. Kocks, C. et al. Eater, a transmembrane protein mediating phagocytosis of bacterial pathogens in *Drosophila*. *Cell* **123**, 335–346 (2005).
24. Ramet, M., Manfruelli, P., Pearson, A., Mathey-Prevot, B. & Ezekowitz, R. A. Functional genomic analysis of phagocytosis and identification of a *Drosophila* receptor for *E. coli*. *Nature* **416**, 644–648 (2002).
25. Philips, J. A., Rubin, E. J. & Perrimon, N. *Drosophila* RNAi screen reveals CD36 family member required for mycobacterial infection. *Science* **309**, 1251–1253 (2005).
26. Stroschein-Stevenson, S. L., Foley, E., O'Farrell, P. H. & Johnson, A. D. Identification of *Drosophila* gene products required for phagocytosis of *Candida albicans*. *PLoS Biol.* **4**, e4 (2006).
27. Mali, P. et al. RNA-guided human genome engineering via Cas9. *Science* **339**, 823–826 (2013).
28. Jinek, M. et al. RNA-programmed genome editing in human cells. *eLife* **2**, e00471 (2013).
29. Cong, L. et al. Multiplex genome engineering using CRISPR/Cas systems. *Science* **339**, 819–823 (2013).
30. Adamson, B. et al. A multiplexed single-cell CRISPR screening platform enables systematic dissection of the unfolded protein response. *Cell* **167**, 1867–1882 e1821 (2016).
31. Koike-Yusa, H., Li, Y., Tan, E. P., Velasco-Herrera Mdel, C. & Yusa, K. Genome-wide recessive genetic screening in mammalian cells with a lentiviral CRISPR-guide RNA library. *Nat. Biotechnol.* **32**, 267–273 (2014).
32. Morgens, D. W. et al. Genome-scale measurement of off-target activity using Cas9 toxicity in high-throughput screens. *Nat. Commun.* **8**, 15178 (2017).
33. Parnas, O. et al. A genome-wide CRISPR screen in primary immune cells to dissect regulatory networks. *Cell* **162**, 675–686 (2015).
34. Shalem, O. et al. Genome-scale CRISPR-Cas9 knockout screening in human cells. *Science* **343**, 84–87 (2014).
35. Wang, T., Wei, J. J., Sabatini, D. M. & Lander, E. S. Genetic screens in human cells using the CRISPR-Cas9 system. *Science* **343**, 80–84 (2014).
36. Zhou, Y. et al. High-throughput screening of a CRISPR/Cas9 library for functional genomics in human cells. *Nature* **509**, 487–491 (2014).
37. Wang, L. et al. High-throughput functional genetic and compound Screens identify targets for senescence induction in cancer. *Cell Rep* **21**, 773–783 (2017).
38. Larrick, J. W., Fischer, D. G., Anderson, S. J. & Koren, H. S. Characterization of a human macrophage-like cell line stimulated in vitro: a model of macrophage functions. *J. Immunol.* **125**, 6–12 (1980).
39. Morgens, D. W., Deans, R. M., Li, A. & Bassik, M. C. Systematic comparison of CRISPR/Cas9 and RNAi screens for essential genes. *Nat. Biotechnol.* **34**, 634–636 (2016).
40. Rotty, J. D. et al. Arp2/3 complex is required for macrophage integrin functions but is dispensable for FcR phagocytosis and in vivo motility. *Dev. Cell.* **42**, 498–513 e496 (2017).
41. Bassik, M. C. et al. A systematic mammalian genetic interaction map reveals pathways underlying ricin susceptibility. *Cell* **152**, 909–922 (2013).
42. Brumell, J. H. et al. Expression of the protein kinase C substrate pleckstrin in macrophages: association with phagosomal membranes. *J. Immunol.* **163**, 3388–3395 (1999).
43. Ma, A. D. & Abrams, C. S. Pleckstrin induces cytoskeletal reorganization via a Rac-dependent pathway. *J. Biol. Chem.* **274**, 28730–28735 (1999).
44. Roux, K. J., Kim, D. I., Raida, M. & Burke, B. A promiscuous biotin ligase fusion protein identifies proximal and interacting proteins in mammalian cells. *J. Cell Biol.* **196**, 801–810 (2012).
45. Bradley, W. D., Hernandez, S. E., Settleman, J. & Koleske, A. J. Integrin signaling through Arg activates p190RhoGAP by promoting its binding to p120RasGAP and recruitment to the membrane. *Mol. Biol. Cell* **17**, 4827–4836 (2006).
46. Jongstra-Bilen, J. & Jongstra, J. Leukocyte-specific protein 1 (LSP1): a regulator of leukocyte emigration in inflammation. *Immunol. Res.* **35**, 65–74 (2006).
47. Schlam, D. et al. Phosphoinositide 3-kinase enables phagocytosis of large particles by terminating actin assembly through Rac/Cdc42 GTPase-activating proteins. *Nat. Commun.* **6**, 8623 (2015).
48. Kihara, A. Very long-chain fatty acids: elongation, physiology and related disorders. *J. Biochem.* **152**, 387–395 (2012).
49. Collins, S. R. et al. Using light to shape chemical gradients for parallel and automated analysis of chemotaxis. *Mol. Syst. Biol.* **11**, 804 (2015).
50. Kajkowski, E. M. et al. beta-Amyloid peptide-induced apoptosis regulated by a novel protein containing a g protein activation module. *J. Biol. Chem.* **276**, 18748–18756 (2001).
51. Jakobsdottir, J. et al. Rare functional variant in TM2D3 is associated with late-onset Alzheimer's disease. *PLoS Genet.* **12**, e1006327 (2016).
52. Stine, W. B., Jungbauer, L., Yu, C. & LaDu, M. J. Preparing synthetic Abeta in different aggregation states. *Methods Mol. Biol.* **670**, 13–32 (2011).
53. Zhang, Y. et al. An RNA-sequencing transcriptome and splicing database of glia, neurons, and vascular cells of the cerebral cortex. *J. Neurosci.* **34**, 11929–11947 (2014).
54. Uusimaa, J. et al. NHLRC2 variants identified in patients with fibrosis, neurodegeneration, and cerebral angiomatosis (FINCA): characterisation of a novel cerebropulmonary disease. *Acta Neuropathol.* **135**, 727–742 (2018).
55. Nishi, K. et al. ROS-induced cleavage of NHLRC2 by caspase-8 leads to apoptotic cell death in the HCT116 human colon cancer cell line. *Cell Death Dis.* **8**, 3218 (2017).
56. Horsthemke, M. et al. Multiple roles of filopodial dynamics in particle capture and phagocytosis and phenotypes of Cdc42 and Myo10 deletion. *J. Biol. Chem.* **292**, 7258–7273 (2017).

Acknowledgements

We thank the members of the Bassik and Barres laboratories for feedback and support throughout, and S. Grinstein, J. Pritchard, J. Pluvinage, and T. Wyss-Coray for helpful suggestions. We thank T. Flores, J. Mulholland and J. Perrino of the Stanford Electron Microscopy facility for excellent assistance with SEM images, and D. Lysko and W. Talbot for experimental advice. This work was supported by the Christopher and Dana Reeve Foundation International Research Consortium on Spinal Cord Injury, the Dr. Miriam and Sheldon G. Adelson Medical Research Foundation, the JPB Foundation, the Novartis Institute of Basic Research, a National Institutes of Health (NIH) grant to B.A.B. (R01 DA015043), a Jane Coffin Childs Fellowship to R.A.K., the Howard Hughes Medical Institute (J.A.T. and D.T.) and the Stanford Medical Scientist Training Program NIH T32-GM007365 (for L.L.), a Kimmel Scholar Award, an NIH Director's New Innovator Award (DP2 HD094656) to S.R.C., an NIH Director's New Innovator Award (1DP2HD084069-01) and Stanford Neuroscience Institute Brain Rejuvenation Project Award to M.C.B., and generous contributions from Vincent and Stella Coates. C.J.B. was supported by the Damon Runyon Cancer Research Foundation (DRG-2125-12).

Author contributions

C.J.B., M.S.H., B.A.B., S.R.C. and M.C.B. conceptualized the study. C.J.B., M.S.H. and D.W.M. generated and analyzed screen data. A.L. assisted in the cloning of sgRNA libraries. K.T. performed FACS-based phagocytosis screening. J.A.O. and B.E. assisted in generating sgRNA-expressing U937 and RAW 264.7 cell lines and clonally derived knockout lines. H.C. and A.T. assisted in performing phagocytosis microscopy assays. J.A.O. made BirA-NHLRC2 construct and prepared samples for mass spectrometry with advice from E.C.; J.C. and L.J. ran mass spectrometry samples and assisted with analysis; E.R. performed neutrophil migration assays with S.R.C.; J.T., D.V., L.L. and R.L. advised on microscopy experiments. R.L. advised on and performed phalloidin microscopy for NHLRC2 knockouts and frustrated phagocytosis assay.

Competing interests

The authors declare no competing interests.

Additional information

Supplementary information is available for this paper at https://doi.org/10.1038/s41588-018-0254-1.

Reprints and permissions information is available at www.nature.com/reprints.

Correspondence and requests for materials should be addressed to C.J.B. or M.C.B.

Publisher's note: Springer Nature remains neutral with regard to jurisdictional claims in published maps and institutional affiliations.

Methods

U937 cell culture and differentiation. U937 cells were acquired from the American Type Culture Collection (CRL-1593.2). Cells were maintained in suspension culture using spinner flasks for library propagation and tissue culture plates for single-gene knockout lines, all in sterile-filtered U937 growth medium (RPMI1640 supplemented with 2 mM glutamine, 100 units ml^{-1} penicillin, 100 mg ml^{-1} streptomycin and 10% heat-inactivated FCS). Cells were cultured in a humidified 37 °C incubator set at 5% CO_2. Cells were passaged two to three times weekly. To generate frozen aliquots, cells were pelleted by centrifugation (300*g*, 7 min, room temperature), suspended in 90% FCS and 10% dimethylsulfoxide (DMSO), and frozen in cell-freezing containers at −80 °C overnight before transfer to liquid nitrogen for long-term storage.

For differentiation, U937 cells were diluted to a density of 1–2 million cells ml^{-1} in U937 growth medium containing phorbol myristate acetate (PMA) to achieve a final concentration of 50 nM PMA. Cells were plated on tissue culture plastic and allowed to differentiate and adhere for 3 d. After differentiation, cells were recovered by harvesting supernatants and trypsinizing adherent cells. For trypsinization, cells were washed three times with PBS (137 mM NaCl, 2.7 mM KCl, 8 mM sodium phosphate dibasic, 2 mM potassium phosphate monobasic, pH 7.4), incubated in PBS containing 300 units ml^{-1} trypsin for 7 min at 37 °C and then recovered from the plate by repeated pipetting of the solution to dislodge cells. Trypsinized adherent and nonadherent supernatant cells were pooled, pelleted by centrifugation (300*g*, 7 min, room temperature) and resuspended in fresh U937 growth medium. Cells were then plated and allowed to recover for 2 d before assays were performed. For screens, 100 million differentiated U937 cells were plated in 100 ml of U937 growth medium in 15 cm tissue culture dishes. For validation assays and other experiments, cells were plated at a density of 500,000 cells ml^{-1} in 96-well plates.

CD11b staining. U937 cells were differentiated in 50 nM PMA as described above, or they were left undifferentiated and 500,000 cells per well were plated in a glass-bottom 24-well plate. On day five post-differentiation cells were washed twice with cold dPBS, blocked with 500 µl 3% BSA in dPBS for 1 h and then incubated for 30 min with 500 µl of a 1:200 dilution of the CD11b antibody (Biolegend, 101202, clone M1/70). Cells were then washed three times with cold dPBS. Secondary antibody (donkey anti-rat AlexaFluor 488, Thermo Fisher, A-21208) was added at a 1:1,000 dilution in Dulbecco's phosphate-buffered saline (dPBS) and incubated in the dark for 1 h. Cells were then washed five times in cold dPBS. Cells were then incubated with a 1:10,000 dilution of Hoechst nuclear stain for 3 min in the dark and washed once with cold dPBS.

RAW 264.7 cell culture. RAW 264.7 cells were acquired from the American Type Culture Collection (TIB-71). Cells were maintained on tissue culture plastic in RAW growth medium (DMEM supplemented with 2 mM glutamine, 100 units ml^{-1} penicillin, 100 mg ml^{-1} streptomycin and 10% heat-inactivated FCS). Cells were passaged by gently lifting the cells with a disposable cell scraper, pelleting by centrifugation (300*g*, 7 min, room temperature) and replating the cells in fresh RAW growth medium.

Library preparation. The 10-sgRNA-per-gene CRISPR/Cas9 deletion library was synthesized, cloned and infected into Cas9-expressing U937 cells as described[32]. Briefly ~300 million U937 cells stably expressing SFFV-Cas9-BFP were infected with the ten-guide-per-gene genome-wide sgRNA library at a multiplicity of infection <1. Infected cells underwent puromycin selection (1 µg ml^{-1}) for 5 d, after which puromycin was removed and cells were resuspended in normal growth medium without puromycin. After selection, sgRNA infection was measured as >90% of cells as indicated by measuring mCherry-positive cells with flow cytometry. Sufficient sgRNA library representation was confirmed by deep sequencing after selection. Selected library-carrying U937 cells were stored in liquid nitrogen, and cells were thawed and expanded for at least 5 d before differentiation for screens.

Generation of individual sgRNA-expressing U937 and RAW 264.7 cell lines. For generating individual sgRNA phenotypes we lentivirally infected U937 cells stably expressing SFFV-Cas9-BFP or RAW 264.7 cells stably expressing EF1Alpha-Cas9-BFP with constructs expressing a given sgRNA along with puromycin resistance. At 3 d after infection we selected with 1 µg ml^{-1} puromycin for U937s and 10 µg ml^{-1} puromycin for RAW 264.7 cells for 5 d. In cases where single-cell clonal knockout lines were derived, after puromycin selection, single cells were sorted into 96-well plates and expanded for 2–3 weeks.

Gene editing measurements by Sanger sequencing. Cells were harvested and total genomic DNA was isolated using QuickExtract DNA Extraction Solution (VWR, QE09050). PCR was prepared using 5× GoTaq Green reaction buffer and GoTaq DNA polymerase (Promega, M3005), 10 mM dNTPs and primers designed about 250–350 bp upstream and 450–600 bp downstream of the predicted cut site. PCR reactions were run on a C1000 Touch Thermo Cycler (Bio-Rad). PCR products were then purified over an Econospin DNA column (Epoch, 1910-250) using buffers PB and PE (Qiagen, 19066 and 19065). Sanger sequencing was performed and applied biosystems sequence trace files (.ab1 files) were obtained from Quintara Biosciences. Editing efficiency of knockout cell lines was analyzed using Synthego's online ICE Analysis Tool.

Phagocytosis substrate preparation. Details for all phagocytosis substrates, IONP labeling reactions and pHrodo labeling reactions are in Supplementary Table 3. Midbeads, SmallBeads, Bigbeads and Posbeads (Spherotech) were stored at 4 °C and pelleted, and then resuspended in PBS before use. Zymosan (Sigma) was suspended to 10 mg ml^{-1} in PBS and then filtered through a 40 µm cell strainer (BD Biosciences) to remove large poorly resuspended material. Myelin was prepared using perfused total brain homogenate from adult rats as described[57]. Myelin concentration was estimated using wet pellet weight, and myelin was stored in single-thaw aliquots of 20–100 mg ml^{-1} at −30 °C. Sheep erythrocytes (RBCs, MP Biomedicals) were opsonized following a published protocol[58] before conjugation of IONPs or pHrodo. Briefly, cells were washed with PBS, incubated with polyclonal rabbit anti-sheep RBC IgG or polyclonal rabbit anti-sheep RBC IgM followed by complement factor 5–depleted serum (C5d serum), and then washed repeatedly before storage at 4 °C in dPBS with calcium and magnesium for up to 4 weeks. For unopsonized, IgM-opsonized, or C5d serum–opsonized RBCs, all wash and incubation steps were performed as for complement-opsonized cells except that IgM and/or C5d serum were omitted as appropriate.

Synaptosomes were prepared using perfused whole brain from adult rats based on density centrifugation as described[59] and stored at −30 °C in single-thaw aliquots.

Amyloid-β aggregates were generated as described[52] by dissolving human β-amyloid(1–42) (Anaspec) in hexafluoroisopropanol, drying, re-dissolving in DMSO, diluting to 200 mM in PBS, and incubating the peptide for 24 h at 4 °C to promote formation of oligomeric amyloid-β aggregates. Amyloid-β aggregates were labeled with pHrodo by adding pHrodo red succinimidyl ester to 200 µM and incubating the mixture at room temperature for 30 min while it was protected from light on a rocker, after which unconjugated pHrodo dye was separated using size-exclusion Bio-Gel P-6 spin columns prewashed in screening media (Bio-Rad). Amyloid-β aggregates were stored at 4 °C and used within 24 h of aggregation. Amyloid-β was added at 15 mM for phagocytosis assays.

IONP and pHrodo conjugation to phagocytosis substrates. Phagocytosis substrates were covalently labeled at free amine groups with 30 nm–diameter IONPs with *N*-succinimidyl ester functionalization (Sigma), with pHrodo red succinimidyl ester (ThermoFisher Scientific) or with pHrodo green STP ester (ThermoFisher Scientific). Except for amyloid-β, substrates were pelleted by centrifugation, resuspended in PBS to a fixed concentration and incubated with a set amount of pHrodo or IONP for 45 min at room temperature with gentle shaking. Centrifugation time, substrate concentration and label concentration varied with each substrate as described in Supplementary Table 3 to optimize particle integrity, prevent particle clumping and maximize sensitivity of downstream assays. Supernatants of the final wash did not have detectable levels of fluorescence from free pHrodo dye, and did not result in $pHrodo^+$ puncta when incubated with phagocytic cells. After magnet or pHrodo conjugation, phagocytosis substrates were stored in PBS at 4 °C for <1 week (IONP conjugation) or <1 month (pHrodo conjugation). RBCs were washed twice immediately before use to remove any lysed cells and minimize risk of heme inhibition of phagocytosis.

MidBeads, SmallBeads and BigBeads lack inherent free amine reactive groups, and so they were sparsely conjugated with putrescine via 1-ethyl-3-(3-dimethylaminopropyl)carbodiimide hydrochloride (EDC, ThermoFisher Scientific) crosslinking before addition of pHrodo. Beads were washed twice in PBS, pH 5.5 (PBS adjusted with HCl) and resuspended to 5% (w/v) in PBS, pH 5.5. The bead suspension was mixed 1:1 with a 1 M putrescine solution before addition of freshly dissolved EDC crosslinker to 1 mg ml^{-1}. Beads were incubated for 2 h at room temperature before being washed three times in PBS (neutral pH) and resuspended for pHrodo conjugation. The EDC concentration was titrated to prevent bead crosslinking and to incorporate the minimal amount of amine groups that allowed for efficient detection of pHrodo signal at pH 5.5 after subsequent bead labeling.

Magnetic separation–based CRISPR screens. U937 cells carrying the sgRNA library were differentiated with 50 nM PMA for 3 d, trypsinized, and replated at 100 million cells per 15 cm dish as described above. After 2 d of recovery in growth medium lacking PMA, cells were washed eight times with dPBS with calcium and magnesium (dPBS+, Gibco). Cell medium was exchanged with 15 ml of serum-free U937 growth medium (U937 growth medium lacking FCS) and returned to the incubator for 5 min. Then, 5 ml of prewarmed serum-free U937 growth medium was added containing phagocytosis substrate at the concentrations described in Supplementary Table 3. Cells were returned to the incubator for a fixed amount of time depending on the prey, as described in Supplementary Table 3.

After phagocytosis, dishes were rinsed ten times with dPBS+ to remove uningested particles. For screens involving RBCs, dishes were exchanged into ACK lysis buffer and swirled for 10 sec to promote RBC lysis before dPBS+ washes. Cells were then exchanged into 15 ml of Medium A and 100 µl of trypsin stock solution (30,000 units per ml stock, Sigma) was added to each plate. Cells were returned to the incubator for 10 min to facilitate cell removal from the culture dish and

substrate removal from the cell surface. After trypsinization, 3 ml of Medium A containing 10 mM $MgCl_2$ was added to each dish to minimize cell lysis and bead aggregation. 40 µl of DNase I stock solution (0.4% DNase, Worthington) was added to each plate to prevent carryover of genomic DNA from lysed cells.

Cells were dislodged from the dish with repeated pipetting and passed through a 40 µm cell strainer (BD Biosciences) to remove aggregated cells. Cells were subsequently agitated periodically to minimize cell settling and potential aggregation. To maximize cell recovery, 12 ml of separation buffer (12 ml of Medium A with 2 mM $MgCl_2$ and 0.1% milk peptone (Sigma)) with 0.001% DNase I was added to each dish and the remaining cells were recovered with a cell scraper. Scraped cells were pipetted repeatedly, passed through a 40 µm cell strainer (BD Biosciences) and combined with pipetted cells.

Next, cells were passed over 4–6 LS magnetic columns (Miltenyi) equilibrated with separation buffer and mounted in the magnetic holder. Only 2 ml of cell suspension was applied to each column at a time, and it was allowed to drain before immediate addition of an additional 2 ml of cell suspension. Column flowthrough was collected and reserved as the unbound fraction. After all of the cell suspension had been loaded, columns were washed three times with 2 ml of separation buffer and flowthrough was combined with the unbound fraction. After three washes, columns were removed from the magnetic apparatus and 3 ml of separation buffer was gently flushed through the demagnetized column with a syringe plunger. The column eluate was reserved as the bound fraction. EDTA was added to achieve a final concentration of 2 mM to each fraction and cells were pelleted by centrifugation (7 min at 300*g*, room temperature). Cells were resuspended in 90% FCS and 10% DMSO with 2 mM EDTA and frozen in cell freezing containers at −80 °C for subsequent genomic DNA extraction.

For pilot experiments and to determine the phagocytosis duration required to capture the majority of U937 cells on the magnet, the above experiments were scaled down to 6-well plates. For cytochalasin D experiments, cytochalasin D was added to 10 µM at 5 min before addition of phagocytosis substrate. After recovery of the bound and unbound fractions, cells were resuspended in dPBS+ containing 1.33 µM calcein AM (Invitrogen) to visualize live cells.

Screen analysis. At the end of each screen genomic DNA was extracted for all screen populations separately according to the protocol included with QIAGEN Blood Maxi Kit. Using known universal sequences present in the lentivirally incorporated DNA, sgRNA sequences were amplified and prepared for sequencing by two sequential PCR reactions as described[39]. Products were sequenced using an Illumina Nextseq to monitor library composition (30–40 million reads per library). Trimmed sequences were aligned to libraries using Bowtie, with zero mismatches tolerated and all alignments from multimapped reads included.

Guide composition and comparisons across bound and unbound fractions were analyzed using casTLE[39] version 1.0. Briefly, for each pair of bound and flowthrough samples, guides with <25 counts in both conditions were removed from the analysis. If a guide had <25 counts in a single condition, this value was changed to be equal to 25 counts. Enrichment of individual sgRNAs was then calculated as a median-normalized log ratio of the fraction of counts, as described[60]. For each gene, a maximum likelihood estimator was used to identify the most likely effect size and associated log-likelihood ratio (confidence score) by comparing the distribution of gene-targeting guides to a background of nontargeting and safe-targeting guides. *P* values were then estimated by permuting gene-targeting guides, and hits were called using FDR thresholds (Supplementary Table 1) calculated via the Benjamini-Hochberg procedure. For small-scale retest and FACS screens, a similar analysis was used except genes were called as hits when their effect score at 95% credible interval did not include zero[61,62] (Supplementary Table 5). Additionally, for small-scale magnetic screens, a count threshold of 100 was used to adjust for higher sequencing coverage. Permutations were not used to calculate *P* values for small-scale retest screens as a large fraction of guides in these screens are expected to have effects on phagocytosis. Two more stringent analyses were also included: (1) requiring genes to pass the 95% credible interval in both individual replicates and (2) analysis of the small-scale retest screening using MAGeCK (ref. [63]; Supplementary Table 5). MAGeCK (version 0.5.6) was run using the 'mageck test' command supplied with the '--norm-method control' option and otherwise with default options.

pHrodo phagocytosis assay. U937 cells were differentiated as described above for magnetic separation. After 3 d of PMA exposure, cells were lifted, centrifuged and re-plated in 96-well tissue culture plates at a density of 50,000 cells per well in 100 µl U937 growth medium. After an additional 2 d of recovery, nonadherent cells were eliminated by being washed twice with dPBS. Then, dPBS was removed and replaced with prewarmed serum-free U937 growth medium (U937 growth medium lacking 10% FBS) containing the appropriate pHrodo-labeled phagocytosis substrate(s) at the concentration denoted in Supplementary Table 3.

Some experiments included cytochalasin D (10 µM) in the serum-free U937 growth medium for select wells. For fatty-acid rescue experiments (Fig. 5), fatty acids (Cayman Chemical) were added first to U937 growth medium used when cells were plated in 96-well plates, and second to serum-free U937 growth medium containing phagocytosis substrates (C18s, stearic acid and oleic acid at 3 µg ml^{-1} each or lignoceric acid and nervonic acid at 3 µg ml^{-1} each, all from ethanol stocks). All cell plating in 96-well plates, washing and addition of phagocytosis substrates were performed using a multichannel pipette.

After addition of phagocytosis substrates, cells were returned to the incubator and imaged at 30–60 min intervals using an Incucyte (Essen). The first time point (reported as $t=0$) was typically acquired within 5–20 min of cells returning to the incubator. Reported values are averaged over four fields per well, with at least four wells used per data point. Images were acquired at ×20 objective at 400 ms (green) or 800 ms (red) exposures per field. After the last imaging time point, calcein-AM (Invitrogen) was added to a final concentration of 1.33 µM. Cells were incubated with calcein-AM for 15 min before a final image acquisition to determine total live cell area per field. No visual decrement in cell survival or health was noticeable after 24 h of imaging in serum-free medium.

To calculate a phagocytic index for each well, the total pHrodo-positive area was determined for each time point and normalized to the total calcein-positive live cell area measured immediately after the 5 h time point. Total area was calculated using automated analysis scripts that performed a fixed-value adaptive background subtraction and selected signal-positive regions that passed intensity thresholds. Different analysis scripts were generated for each phagocytosis substrate to accurately report signal from ingested material. Cellular localization and accurate selection of pHrodo or calcein signal were confirmed visually.

For phagocytosis assays with RAW 264.7 cells, cells were plated at 25,000 cells per well of a 96-well plate. One day later, cells were washed twice with dPBS and exchanged into serum-free RAW cell growth medium. For cells transduced with constitutively active Rac1, Rac1 expression was induced by addition of 5 ng ml^{-1} doxycycline at the time of transfer to 96-well plates and doxycycline was removed upon transfer to serum-free medium for phagocytosis assays. RAW 264.7 cell phagocytosis was imaged and analyzed as for U937 cells.

For additional methods see Supplementary Note.

Reporting Summary. Further information on research design is available in the Nature Research Reporting Summary linked to this article.

Code availability. casTLE version 1.0 is available at https://bitbucket.org/dmorgens/castle.

Data availability

The RNA-seq FASTQ files are available at GEO under accession GSE107566.

References

57. Larocca, J. N. & Norton, W. T. Isolation of myelin. *Curr. Protoc. Cell. Biol.* **Chapter 3**, Unit 325 (2007).
58. Mosser, D. M. & Zhang, X. Measuring opsonic phagocytosis via Fcgamma receptors and complement receptors on macrophages. *Curr. Protoc. Immunol.* **Chapter 14**, Unit 14 27 (2011).
59. Dunkley, P. R., Jarvie, P. E. & Robinson, P. J. A rapid Percoll gradient procedure for preparation of synaptosomes. *Nat. Protoc.* **3**, 1718–1728 (2008).
60. Kampmann, M., Bassik, M. C. & Weissman, J. S. Integrated platform for genome-wide screening and construction of high-density genetic interaction maps in mammalian cells. *Proc. Natl Acad. Sci. USA* **110**, E2317–E2326 (2013).
61. Kramer, N. J. et al. CRISPR-Cas9 screens in human cells and primary neurons identify modifiers of C9ORF72 dipeptide-repeat-protein toxicity. *Nat. Genet.* **50**, 603–612 (2018).
62. Liu, N. et al. Selective silencing of euchromatic L1s revealed by genome-wide screens for L1 regulators. *Nature* **553**, 228–232 (2018).
63. Li, W. et al. MAGeCK enables robust identification of essential genes from genome-scale CRISPR/Cas9 knockout screens. *Genome. Biol.* **15**, 554 (2014).

nature research

Corresponding author(s): Michael Bassik and Christopher Bohlen

☐ Initial submission ☐ Revised version ☒ Final submission

Life Sciences Reporting Summary

Nature Research wishes to improve the reproducibility of the work that we publish. This form is intended for publication with all accepted life science papers and provides structure for consistency and transparency in reporting. Every life science submission will use this form; some list items might not apply to an individual manuscript, but all fields must be completed for clarity.

For further information on the points included in this form, see Reporting Life Sciences Research. For further information on Nature Research policies, including our data availability policy, see Authors & Referees and the Editorial Policy Checklist.

Experimental design

1. Sample size

Describe how sample size was determined. Not done

2. Data exclusions

Describe any data exclusions. No data was excluded.

3. Replication

Describe whether the experimental findings were reliably reproduced. Once experiments and procedures were fully optimized, all attempts at replication were successful. To ensure reproducibility every experiment performed in replicate. Number of replicates for each experiment is indicated in figure legends.

4. Randomization

Describe how samples/organisms/participants were allocated into experimental groups. U937 and RAW 264.7 KO clones were allocated into experimental groups based on their genotype (Extended Data Figure 5ab)

5. Blinding

Describe whether the investigators were blinded to group allocation during data collection and/or analysis. Blinding was performed in assessing scanning electron microscopy images.

Note: all studies involving animals and/or human research participants must disclose whether blinding and randomization were used.

6. Statistical parameters

For all figures and tables that use statistical methods, confirm that the following items are present in relevant figure legends (or in the Methods section if additional space is needed).

n/a	Confirmed
☐	☒ The exact sample size (*n*) for each experimental group/condition, given as a discrete number and unit of measurement (animals, litters, cultures, etc.)
☐	☒ A description of how samples were collected, noting whether measurements were taken from distinct samples or whether the same sample was measured repeatedly
☐	☒ A statement indicating how many times each experiment was replicated
☐	☒ The statistical test(s) used and whether they are one- or two-sided (note: only common tests should be described solely by name; more complex techniques should be described in the Methods section)
☐	☒ A description of any assumptions or corrections, such as an adjustment for multiple comparisons
☐	☒ The test results (e.g. *P* values) given as exact values whenever possible and with confidence intervals noted
☐	☒ A clear description of statistics including central tendency (e.g. median, mean) and variation (e.g. standard deviation, interquartile range)
☐	☒ Clearly defined error bars

See the web collection on statistics for biologists for further resources and guidance.

Software

Policy information about availability of computer code

7. Software

Describe the software used to analyze the data in this study.	For screen analysis we used custom Python scripts available at https://bitbucket.org/dmorgens/castle (see methods section, 'Magnetic-separation based CRISPR screens' and "FACS Screen'). For image analyses we used Python 2.7.12, Prism 7.0b (Graphpad), Cytoscape 3.5.1, and R 3.3.2. Incucyte ZOOM software (Essen) was used for automated microscopy analysis. Flowjo 9.9 was used for flow cytometry analyses. RNA-seq data was mapped tusing HISAT2 version 2.0.3 (Kim et al., 2015) via the Galaxy platform (https://usegalaxy.org/) (Afgan et al., 2016), and Cufflinks version 2.2.1 (Trapnell et al., 2010). ImageJ 1.5i (https://imagej.nih.gov/ij/). MAGeCK version 0.5.6 (https://bioweb.pasteur.fr/packages/pack@mageck@0.5.6). Thermo Proteome Discoverer software version 2.2 (https://www.thermofisher.com/order/catalog/product/OPTON-30795).

For manuscripts utilizing custom algorithms or software that are central to the paper but not yet described in the published literature, software must be made available to editors and reviewers upon request. We strongly encourage code deposition in a community repository (e.g. GitHub). *Nature Methods* guidance for providing algorithms and software for publication provides further information on this topic.

Materials and reagents

Policy information about availability of materials

8. Materials availability

Indicate whether there are restrictions on availability of unique materials or if these materials are only available for distribution by a for-profit company.	No restrictions.

9. Antibodies

Describe the antibodies used and how they were validated for use in the system under study (i.e. assay and species).	anti -BSA IgG: ASBSA-GF (Molecular Innovations) CD11b antibody: Biolegend - Cat # 101202, Clone M1/70, 1:200 dilution donkey anti-rat AlexaFluor 488, Thermo Fisher Cat # A-21208, 1:1000 dilution

10. Eukaryotic cell lines

a. State the source of each eukaryotic cell line used.	Cell lines are from commercial sources. U937: ATCC RAW 264.7: ATCC
b. Describe the method of cell line authentication used.	Cell lines were authenticated by the vendor (ATCC). Authentication includes an assay to detect species specific variants of the cytochrome C oxidase I gene (COI analysis) to rule out inter-species contamination and short tandem repeat (STR) profiling to distinguish between individual human cell lines and rule out intra-species contamination.
c. Report whether the cell lines were tested for mycoplasma contamination.	Cell cultures were routinely tested and found negative for mycoplasma infection (MycoAlert, Lonza).
d. If any of the cell lines used are listed in the database of commonly misidentified cell lines maintained by ICLAC, provide a scientific rationale for their use.	None of the cell lines used in this study are in the database of commonly misidentified cell lines.

Animals and human research participants

Policy information about studies involving animals; when reporting animal research, follow the ARRIVE guidelines

11. Description of research animals

Provide details on animals and/or animal-derived materials used in the study.	No animals were used in this study.

Policy information about studies involving human research participants

12. Description of human research participants

Describe the covariate-relevant population characteristics of the human research participants.	This study did not involve human research participants.